ELSEVIER

Journal of Structural Geology 30 (2008) 98–115

JOURNAL OF STRUCTURAL GEOLOGY

www.elsevier.com/locate/jsg

Deformation, exhumation, and topography of experimental doubly-vergent orogenic wedges subjected to asymmetric erosion

Leonardo Cruz [a,*], Christian Teyssier [a], Lesley Perg [a], Andy Take [b], Annia Fayon [a]

[a] *Department of Geology and Geophysics, University of Minnesota, Minneapolis, MN 55455, USA*
[b] *Civil Engineering, Queen's University, Kingston, ON K7L 3N6, Canada*

Received 3 February 2007; received in revised form 22 October 2007; accepted 25 October 2007
Available online 7 November 2007

Abstract

We explore the effect of asymmetric erosion and dip angle of the indenter on the internal kinematics, deformation, and exhumation of an experimental doubly-vergent orogenic wedge during transient and steady-state flux conditions. We calculate displacement fields and derive strain and exhumation for several erosion and non-erosion cases, using particle image velocimetry (PIV) analysis. We apply calculated displacement fields to a simple heat equation to explore virtual evolution of thermal structure. Erosion exerts a primary control in the internal kinematics of the experimental wedge. In non-erosion cases, early-formed fore-shears rotate toward the indenter, such that the shear bands become steeper. This effect is more pronounced in prowedge erosion cases, where shear bands become very steep and even overturned. Conversely, retrowedge erosion results in back rotation of early-formed fore-shears, and the shear bands evolved to gently dipping structures. Wedge erosion, in combination with the condition of flux and topographic steady-state, increases density of fore-shears, and controls size, width, and topographic divide migration. Steeply dipping indenters produce overall gentle particle trajectories, and gently dipping indenters favor steep trajectories. Particle velocity, with respect to isotherms, increases where erosion is concentrated and near active fore-shears.

Keywords: Orogenic wedge; Asymmetric erosion; Sandbox Modeling; Exhumation; Kinematics; PIV

1. Introduction

The interaction and feedback between tectonics and surface processes in orogens have been suspected since early studies of thrust tectonics (Chapple, 1978; Suppe, 1981; Davis et al., 1983; Dahlen, 1984; Dahlen and Suppe, 1988) and is currently an extensive topic of research (Beaumont et al., 1992, 2001; Willett, 1999). Mountain building and erosion are two competing processes. Mountain building creates topography, and erosion destroys it. Through erosional processes, mass can be transported and redistributed at the Earth's surface, which modifies the gravitational load and alters the stress field and kinematics within orogens (Dahlen and Suppe, 1988; Koons, 1990; Willett, 1999).

Orogenic wedges are defined as masses of rock with wedge shape underlain by a basal décollement. Wedge mechanics is comparable to that of a sand or snow wedge being pushed by a bulldozer (Suppe, 1981). During the cross-sectional growth of a wedge and once a critical slope or a taper angle is attained, which is dependent on friction along the basal décollement and the internal rheology, the wedge slides over the basal décollement with little or no internal deformation. Therefore, any surface process that alters the critical slope in the way of removal of material or redistribution of masses will affect the internal evolution of the wedge. One of these surface processes, erosion, is reported to play an important role in orogenic exhumation, deformation, and thermal evolution (Dahlen and Barr, 1989; Barr and Dahlen, 1989; Willett et al., 1993; Avouac and Burov, 1996; Willett, 1999; Zeitler et al., 2001; Willett and Brandon, 2002; Jamieson et al., 2002; Finlayson et al., 2002; Reiners et al., 2002).

* Corresponding author. Tel.: +650-723-0848; fax: +650-725-0979.
E-mail addresses: leocruz@stanford.edu, leo@cruzhernandez.net (L. Cruz).

0191-8141/$ - see front matter © 2007 Elsevier Ltd. All rights reserved.
doi:10.1016/j.jsg.2007.10.003

In orogens, the condition of flux steady-state is achieved when a balance exist between erosional flux and accretionary flux (Brandon et al., 1998; Pazzaglia and Brandon, 2001; Willett and Brandon, 2002). This condition is different to topographic steady-state (Willett and Brandon, 2002), which refers to the condition in which all the points of the Earth's surface remain at the same elevation with time. The ideal condition of flux steady-state may not be attained in natural systems, although this condition has been proposed for different active orogens such as Taiwan (Suppe, 1981), the Southern Alps of New Zealand (Adams, 1980), and the Olympic Mountains (Brandon et al., 1998; Pazzaglia and Brandon, 2001).

Several numerical models (Koons, 1987; Beaumont et al., 1992; Willett et al., 1993; Willett, 1999; Willett and Brandon, 2002; Jamieson et al., 2002) have used spatially focused erosion to study the feedback between tectonic and surface processes in orogens. Spatially focused erosion, which is similar to having a climatically wet and a dry side of an orogen due to prevailing winds, may result in localization of deformation and exhumation, isotherm advection, and migration of the topographic divide. Similarly, analogue experimental models have shown that wedge erosion, which has been applied asymmetrically in some cases, leads to rapid uplift/exhumation (Koons, 1990), high-grade metamorphic peak profiles (Koons, 1990), fault reactivation (Koyi et al., 2000; Leturmy et al., 2000), steepening of the faults (Cobbold et al., 1993; Persson et al., 2004), expansion of the duration of activity on single faults (Merle and Abidi, 1995; Cobbold et al., 1993; Persson and Sokoutis, 2002; Persson et al., 2004), and delay in the propagation of deformation (Hoth et al., 2006). However, these analogue experiments, except the work of Hoth et al. (2006), lack precise quantification of the internal displacement field to derive highly detailed maps of strain and exhumation and to monitor evolution of an orogen. Furthermore, none of these previous experiments monitored deformation and exhumation during the transient and steady-state conditions of flux and topography that represent the latest state of a dynamically coupled orogenic system (Willett and Brandon, 2002), except the work of Konstantinovskaia and Malavieille (2005) that imposed a flux steady-state condition with a different erosion rule from the one used in this study.

Quantification of particle trajectories within orogens is essential to understanding deformation and exhumation processes in mountain belts. Several studies have found complexity in the particle trajectories within experimental and analytical models of orogens (Koons, 1990; Mulugeta and Koyi, 1992; Stüwe and Barr, 1998), and the thermochronologic implications of those complex trajectories are significant when calculating exhumation rates and patterns (Batt and Brandon, 2002). The questions of how rock moves up to the surface and how long it resides at a specific structural level are key to understanding the evolution of orogens, and particularly doubly-vergent orogenic wedges.

In this paper, we explore the effect of asymmetric erosion on the internal structure of an experimental doubly-vergent orogenic wedge during transient and steady-state flux conditions. The doubly-vergent orogenic wedge is represented by a wedge of non-cohesive, dry Coulomb material, walnut shells, which has not been used before in experimental modeling of tectonic wedges. We test and characterize the frictional properties of the walnut shells. We use two indenter geometries to compare and evaluate the evolving patterns of deformation and exhumation between models as a function of dip angle, since indenter dip is proposed to affect deformation and exhumation patterns in natural orogens such as the Central Alps (Bonini et al., 1999) and the backbone range of Taiwan (Yui and Chu, 2002). We calculate the displacement field in the wedge, from which we derive strain and exhumation patterns, using particle image velocimetry (PIV) analysis. In our experimental setting, erosion is controlled, and exhumation, deformation, and topography are unconstrained variables that evolve in response to the processes taking place within the wedge and at the surface. Additionally, we coupled the experimentally derived displacement field to a simple heat equation to analytically explore the virtual thermal evolution of an erosional orogenic wedge.

2. Experimental setup

2.1. Materials

Granular materials, such as sand, are used extensively in scaled sandbox experiments since they reproduce mechanical behaviors believed to occur in the earth crust, i.e. distributed deformation followed by shear localization in narrow zones during failure process (Lohrman et al., 2003). In our experiment, we decided to use and test crushed dry walnut shells instead of the more widely used sand for two reasons. First, density of walnut shells is lower than that in sand, allowing us to increase the height of the deforming layer according to scaling parameters and better resolve shear zones by PIV. Second, walnut shells are less abrasive than sand, which increase accuracy of the PIV technique by reducing scratches on the surface of the lateral Plexiglas panel of the experimental apparatus. We later found that our general model evolution and walnut-shell deformation behavior are consistent with those described in sand models by Malavieille (1984); Colletta et al. (1991); Bonini et al (1999), and Persson and Sokoutis (2002).

The apparatus, a Plexiglas–aluminum experimental box (Fig. 1A), was filled with crushed dry walnut shells of ~0.5 mm diameter, bulk density of 750 kg/m^3, friction angle of 38.5–40.8 ° and cohesion of 23 ± 13 Pa (Appendix A) to create a continuous 5 cm thick horizontal layer. The walnut shell particles were sprinkled into the experimental box from a fixed height of 13 cm from the base of the model, leveled and compacted by placing a dead weight of 1.5 kg on top of the walnut shell layer to guarantee homogeneous initial material conditions. This filling and compacting technique was reproduced in all the experimental runs.

Recent scaled sandbox studies show that location of observation (i.e. sidewall versus internal view) and width of the model, especially relatively narrow models, may yield different results (Mandl, 1988; Schreurs et al., 2006), and the

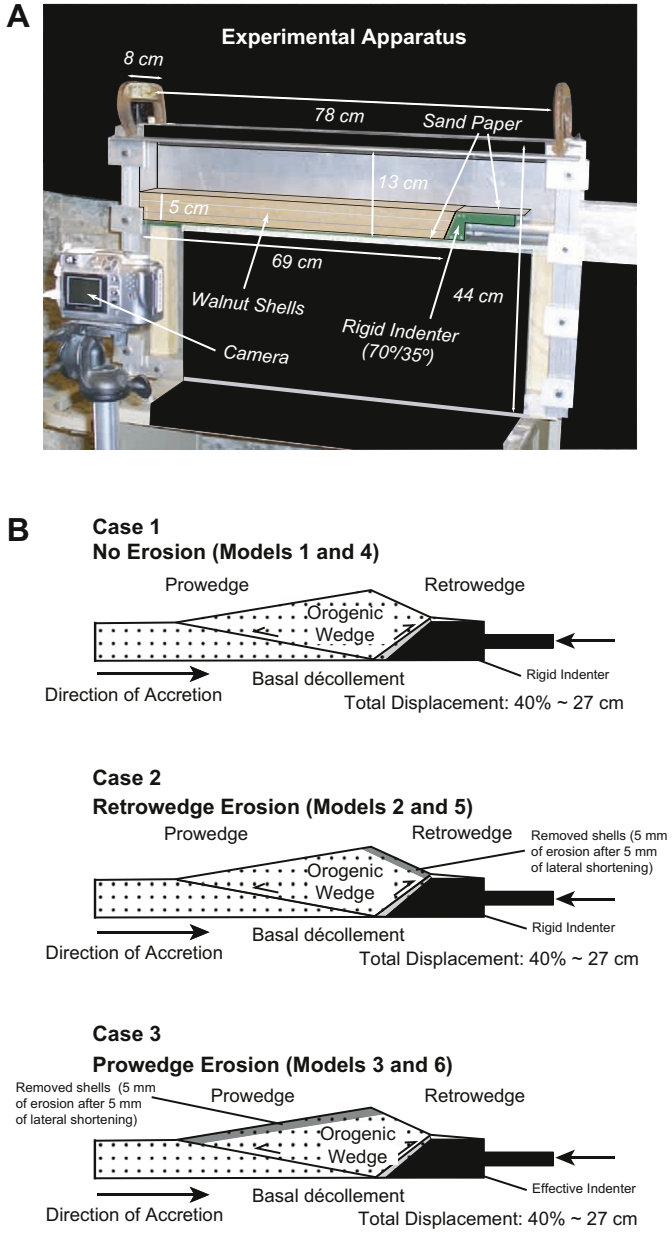

Fig. 1. (A) Experimental setup. Plexiglas–aluminum experimental box filled with a continuous horizontal layer of dry walnut shells. Plexiglas rigid indenters with dip angle of 35 ° and 70 ° were used to deform the horizontal walnut shells layer. (B) Diagram of the experimental setup showing three cases: case 1, non-erosion; case 2, retrowedge erosion; and case 3, prowedge erosion. A thin 5 mm layer of walnut shells was removed from either the prowedge or retrowedge after every 5 mm of lateral displacement. Erosion was initiated after 25 mm of lateral displacement.

electrostatic effect may be significant. The dimensions of the experimental box are 78 cm long, 44 cm high, and 8 cm wide, with a basal dip of 0 ° (Fig. 1A). The size of the box proved large enough so that the lateral frictional effect was minimized and the lateral trend of structures were nearly constant across the width of the experiment (Fig. 3B). A similar sandbox width was used in the experimental setting of Konstantinovskaia and Malavieille (2005) and the frictional sidewall effect was not significant. However, in a strict sense, our model results are only valid at the sidewall.

Five centimeter high rigid (Plexiglas) indenters with dip angle of 35 ° and 70 ° were driven toward the horizontal walnut shell layer at a displacement rate of approximately 0.1 mm/s. However, failure envelop of Coulomb materials (e.g., walnut shells) are independent of strain rate (Davis et al., 1983; Sonder and England, 1986). Therefore, the rate of displacement is not a fundamental variable in our model. The top of the basal surface and the indenters were covered with P400 sand paper to guarantee constant basal friction in our Plexiglas–aluminum experimental box. The internal friction angle of the walnut shells against the P400 sand paper is 35.6–36.7 ° and the cohesion is 80 ± 13 Pa (Appendix A). This experimental setup assumes that the forces are transmitted laterally into the modeled lithosphere (Peltzer and Tapponnier, 1988; England and Houseman, 1986) and the orogen is driven by indentation rather than basal pull or drag of the subducting plate (Malavieille, 1984; Willett et al., 1993; Ellis, 1995; Hoth et al., 2006). Other limitations of our model include lack of thermal feedback after localization of exhumation and deformation (Beaumont et al., 2001; Zeitler et al., 2001; Koons et al., 2002), absence of isostatic response after thickening or thinning of the crust, lack of ductile strain, abnormally high topographic slopes when compared to nature, which influences isotherms distribution (Stüwe and Barr, 1998), and the assumption that erosion processes are dominated by our erosion rule.

2.2. Scaling

Scaling parameters were calculated using the approach introduced by Hubbert (1937) and successively used by others in analogue modeling (Ramberg, 1967; Cobbold et al., 1993; Koyi, 1997; Schellart, 2000; Persson and Sokoutis, 2002; Lohrman et al., 2003; Persson et al., 2004). In this approach, both model and nature are dynamically similar. Therefore, cohesion is scaled similar to stresses. This relationship is expressed in the following equation (Schellart, 2000):

$$\frac{C^{\mathrm{m}}}{C^{\mathrm{n}}} = \frac{\sigma_{\mathrm{v}}^{\mathrm{m}}}{\sigma_{\mathrm{v}}^{\mathrm{n}}} = \frac{\rho^{\mathrm{m}} \times L^{\mathrm{n}} \times g^{\mathrm{m}}}{\rho^{\mathrm{n}} \times L^{\mathrm{n}} \times g^{\mathrm{n}}} \quad (1)$$

where C is cohesion, σ_{v} is vertical stress, ρ is density, L is length, g is acceleration due to gravity, and the superscript m and n stand for model and nature, respectively.

The 5 cm thick layer of walnut shells represents 10–15 km of continental crust, which gives a length model/nature ratio of 3.3×10^{-6}. The assumed density of the continental crust is 2700 kg/m^3, which gives a density model/nature ratio of 0.27. The gravity ratio is 1, since the experiment was performed in a normal gravity field. Therefore, the calculated scale factor for vertical stresses is 9.25×10^{-7}, which implies a value of ~25 MPa for cohesion of natural crustal rocks and is representative of the Earth's upper crust (Goodman, 1988), given the measured cohesion of 23 Pa for the walnut shells.

2.3. Procedure

We present six models. The walnut shell layer in models 1–3 and 4–6 were deformed with a 70 ° and 35 ° dipping indenter, respectively. The height of the rigid indenter and the walnut shell layer were similar in all the experiments. Therefore, the analogue ''continental crust'' was able to deform in the direction of the rigid indenter and over it, forming a doubly-vergent orogenic wedge (Koons, 1990). Two end-member erosion scenarios were considered in this study (Fig. 1B) in addition to a non-erosion case for reference. In the first case (models 1 and 4), erosion was not applied during deformation. In the second case (models 2 and 5), erosion was concentrated solely on the indenter's side of the orogen or retrowedge of Willett et al. (1993). In the third case (models 3 and 6), erosion was focused on the flank opposite to the indenter's side or prowedge of Willett et al. (1993).

Several erosion laws such as constant erosion rate (Dahlen, 1988; Dahlen and Barr, 1989), erosion proportionally linear to elevation (Dahlen and Suppe, 1988), and stream-power river incision (Howard, 1994; Whipple and Tucker, 1999) are used in analytical models of orogens to approximate natural erosion processes. However, accurate application of sophisticated erosion laws to physical experiments remains a challenge because it requires human intervention. Despite this limitation, several erosion rules have been applied to investigate the effect of erosion on several aspects of the evolution experimental orogenic wedges. Cobbold et al. (1993) applied horizontal erosion surfaces to topographic highs at different erosion rates. Persson and Sokoutis (2002) applied constant horizontal erosion surfaces at different erosion rates with material redeposition. They also conducted one experiment with erosion and redeposition in the retrowedge. Konstantinovskaia and Malavieille (2005) imposed constant inclined erosion surfaces determined by the taper of a reference non-erosion wedge without material redeposition. Hoth et al. (2006) used a linear elevation-dependent erosion rate focused either in the prowedge or retrowedge without material redeposition. We will later compare our results with those obtained by Persson and Sokoutis (2002), given the similarities in their boundary conditions with those in our models.

Our erosion rule was spatially constant at a single time step (Fig. 1B) and allowed the achievement of the conditions of flux steady-state in the models after ~40–50% of the total lateral displacement (shortening). The particles were removed with a scraper, using a trajectory approximately parallel to the natural slope that formed from the topographic divide to the level of the top of the rigid indenter in either side of the wedge after each interval of lateral displacement (i.e. if a differential uplift rate developed across the orogen, the topographic profile changed accordingly). We applied this erosion rule because we were interested in both exploring the effect of asymmetric erosion in orogens and allowing the slope of the wedge to evolve relatively unconstrained and achieve flux steady-state conditions, rather than modeling erosion processes. We measured and plotted the area of the growing orogen from the digital images to ensure this condition.

Erosion was initiated after 25 mm of lateral displacement to allow topographic uplift before the application of the first erosion wave. This erosion technique did not produce any noticeable disturbance in the particles below the erosion surface. Each experiment was performed twice to assure reproducibility. The models were deformed up to ~40% of the total length of the deforming layer, which is equivalent to ~27 cm. High-resolution digital images were taken after every millimeter of lateral displacement.

2.4. Particle image velocimetry (PIV)

PIV was used in these experiments to quantify the velocity field and derive strain and exhumation (Fig. 2). PIV is

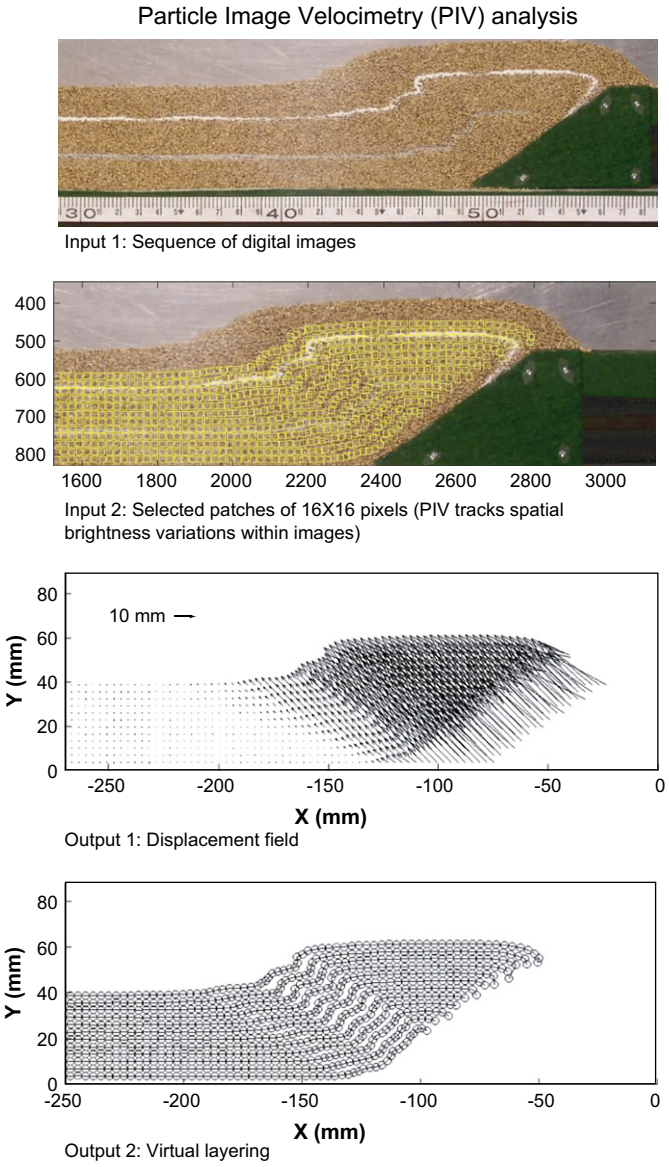

Fig. 2. Particle image velocimetry (PIV) method. PIV procedure includes selection of an initial patch in a first image and a search patch in a final image. Spatial brightness variations within the images are tracked through the image sequence. PIV output may include: displacement field (shown in this figure), virtual layering (shown in this figure), strain, and exhumation.

a technique developed in the field of fluid dynamics to characterize flows in two dimensions (Raffel et al., 1998). PIV has been applied successfully to study granular mechanical processes in scaled experiments (Adam et al., 2002; Adam et al., 2005; Hoth et al., 2006). In our experiment we used GeoPIV, which is a MATLAB module developed by White et al. (2003) that uses the principles of PIV applied to geotechnical testing. This non-commercial module uses textural differences (i.e. brightness variation) within a series of images to derive velocity field with subpixel accuracy (<0.1 pixel). Therefore, under similar boundary conditions, PIV results may be compared directly to 2-D numerical simulations. In our model, one pixel is equivalent to ~0.15 mm, giving an accuracy of ~0.015 mm, which is greater than needed for the desired quantification considering the grain size of ~0.5 mm. PIV calculates and evaluates textural correlation between individual patches from a first image and larger search patches from a second image. The highest correlation peak denotes the position of the displaced patch and corresponding vector (White et al., 2003). We developed several modules within GeoPIV to calculate and visualize cumulative strain and exhumation from the raw PIV velocity field.

3. Results

Models deform as a combination of lateral compaction, localization of strain in shear bands, and slip along the basal décollement. As reported in previous analogue experiments with various boundary conditions (Malavieille, 1984; Koons, 1990; Colletta et al., 1991; Bonini et al., 1999; Persson and Sokoutis, 2002), in the early stages of deformation a ''pop-up'' structure develops, bounded by an active back-shear (i.e. structures that propagates backward toward the indenter or retrowedge side) and an active fore-shear (i.e. structures that propagate forward away from the indenter or toward the prowedge side). This ''pop-up'' structure defines the actively deforming orogenic wedge (Figs. 1B and 3A) whose internal mechanics have been described by Koons (1990), based on the original bulldozer model of Davis et al. (1983) and Dahlen et al. (1984), in which the indenter was infinitely high relative to the deforming material. As deformation continues, a new fore-shear develops and the previous one becomes inactive or ''passive'' and moves back toward the indenter (Malavieille, 1984; Bonini et al., 1999) to form a series of ''thrust'' imbricates (Fig. 3B). The previously formed fore-shear is passive in the sense that the shear zone is not longer active, and it is translated and back-rotated (Mulugeta and Koyi, 1987, 1992; Liu et al., 1992; Koyi, 1995) with little or not deformation according to the overall velocity field of the deforming wedge.

3.1. Shear band evolution

3.1.1. Active fore-shears

Results are summarized in the diagrams of Figs. 4 and 5. When comparing models deformed with similar indenter geometries, non-erosion models produce one fewer shear band than erosion models (Fig. 4). Models deformed with the 35 ° dipping indenter produce more shear bands than those deformed with the 70 ° dipping indenter. Initial dip angle of (active) fore-shears decreases progressively in the non-erosion models (Fig. 4A and D), and it also decreases but remains constant after flux steady-state in the erosion models (Fig. 4B, C, E and F).

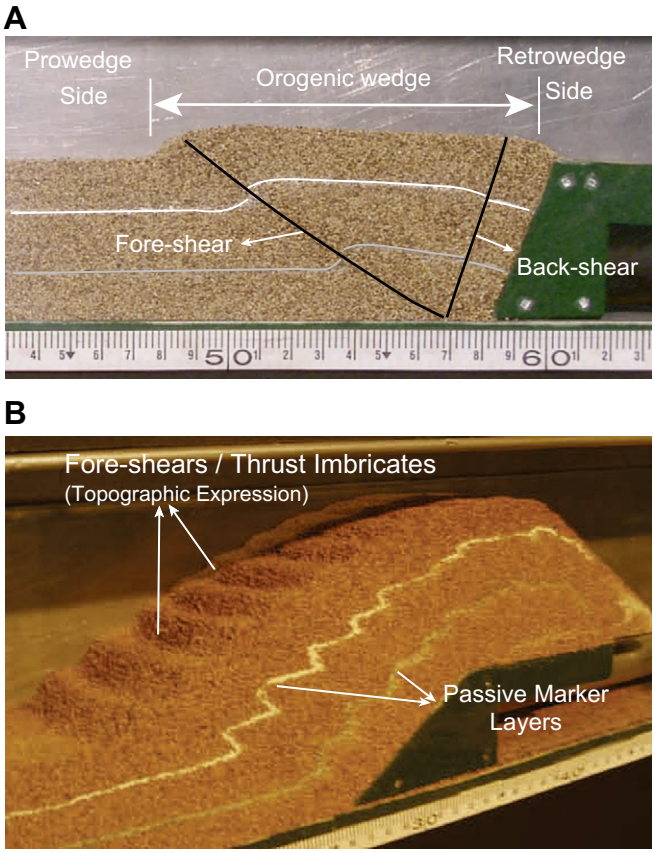

Fig. 3. (A) Photograph of the model showing the development of the doubly-vergent orogenic wedge limited by a fore-shear in the front and a back-shear in the back. We did not observe significant smearing in the walnut shells. (B) Photograph during late stages of lateral deformation showing a series of ''thrust'' imbricates and the slightly arched shape of the strike of the thrusts due to sidewall frictional effect.

To study the relative duration of the activity and the formation of the fore-shears with respect to the lateral displacement of the rigid indenter (shortening) between the models, we recorded and plotted the amount of shortening between initiation and extinction of fore-shears (Fig. 5), given that fore-shears are neither reactivated nor simultaneously active in our models. We called this variable spacing. The spacing tends to increases in all the models (Fig. 5). However, in the erosion models this value becomes relatively constant when the models reach the condition of flux steady-state (Fig. 5B, C, E and F). The spacing in models deformed with the 35 ° dipping indenter is always less than that observed in the 70 ° dipping indenter models. The instant of initiation and extinction of the shear bands was determined directly from the inspection of the digital images.

3.1.2. Passive fore-shears

Fore-shears in non-erosion and prowedge erosion models rotate clockwise toward the indenter (Fig. 6A, C, D and F),

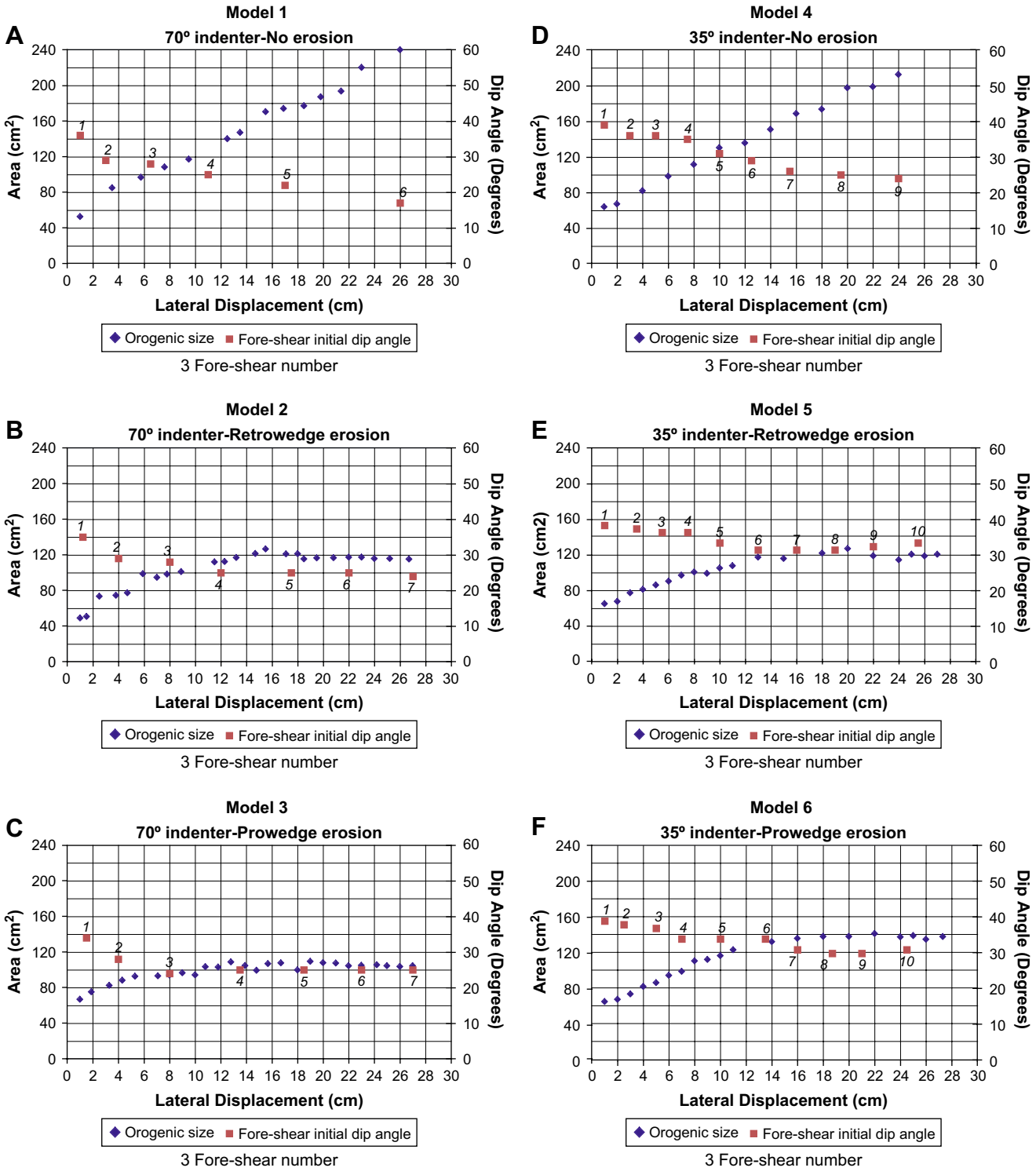

Fig. 4. Plots of the size of the orogenic wedge and the initial dip angle of formation of fore-shears versus lateral displacement. Dips are derived from a visual best-fit line drawn along the fore-shears. Note continuous increase in the size of the orogen in models 1 and 4 (A,D), whereas in models 2, 3, 5, and 6, the orogen reached steady-state (flux steady-state) after ~10–12 cm of lateral displacement (B,C,E,F). Note continuous decrease in the initial dip angle of formation of fore-shears in models 1 and 4 (A,D), whereas in models 2, 3, 5, and 6, the initial dip angle of formation of fore-shears reached a constant value after ~10–12 cm of lateral displacement (B,C,E,F). Stabilization of the initial dip angle coincides with the beginning of the condition of flux steady-state. Fore-shear numbers are shown in chronologic order.

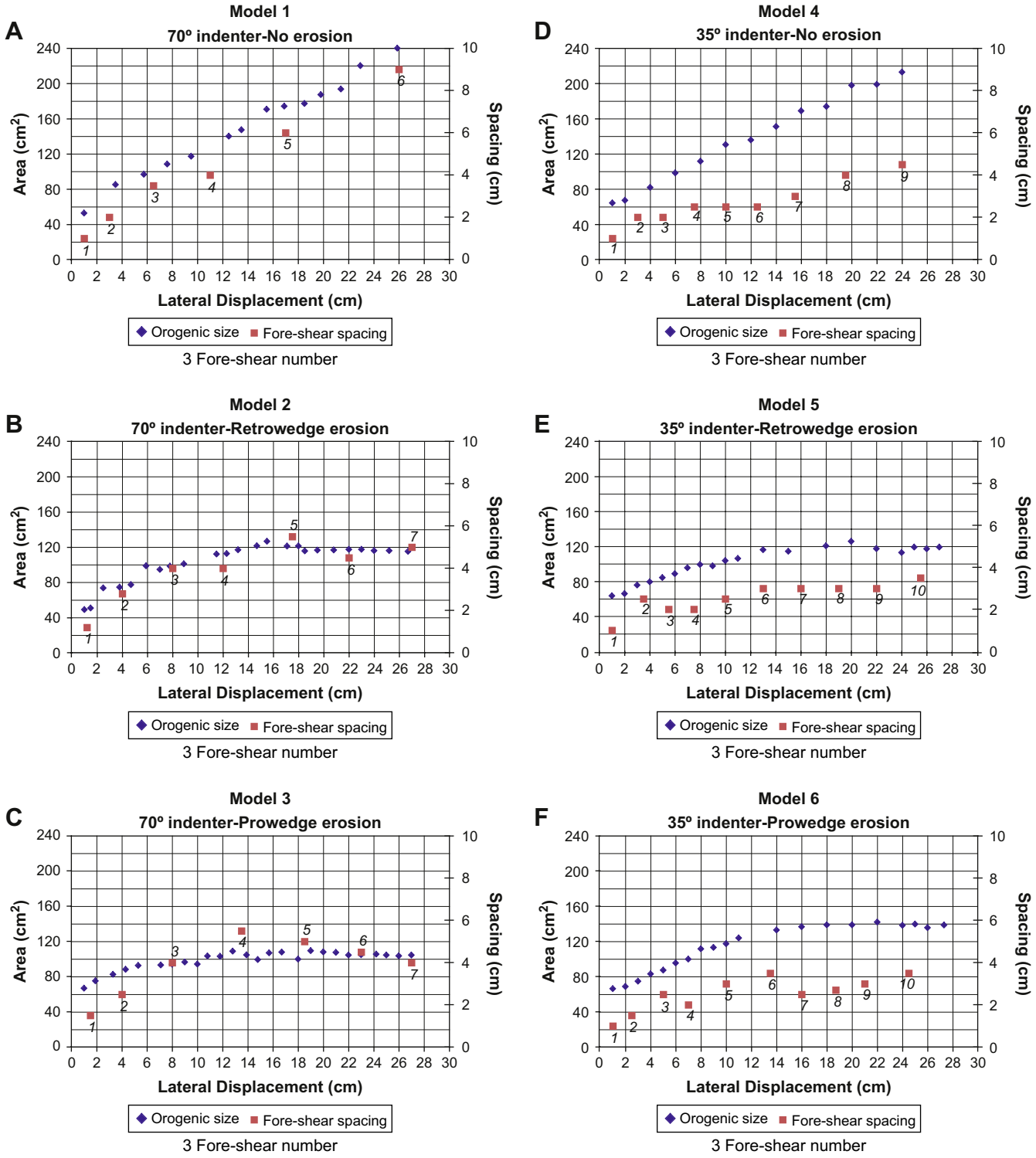

Fig. 5. Plots of the size of the orogenic wedge (referenced to the vertical left axes) and fore-shear spacing, which is the amount of displacement between the initiation of a fore-shear and its extinction (referenced to the vertical right axes), versus lateral displacement (horizontal axes). Note continuous increase in the spacing between fore-shears in the non-erosion models 1 and 4 (A,D), whereas in the erosion models 2, 3, 5, and 6, spacing reached a relatively constant value after ~10–12 cm of lateral displacement (B,C,E,F). Stabilization of the spacing coincides with the beginning of the condition of flux steady-state. Fore-shear numbers are shown in chronologic order.

assuming an observer looking toward the images. Therefore, fore-shears may evolve to steeply dipping or overturned structures on the retrowedge side of those models (Fig. 6C and F). In models deformed with the 70 ° dipping indenter, significant clockwise rotation occurred earlier than in models deformed with the 35 ° dipping indenter. In prowedge erosion models, fore-shears experience a faster clockwise rotation rate than that observed in the non-erosion models (Fig. 6A, C, D and F).

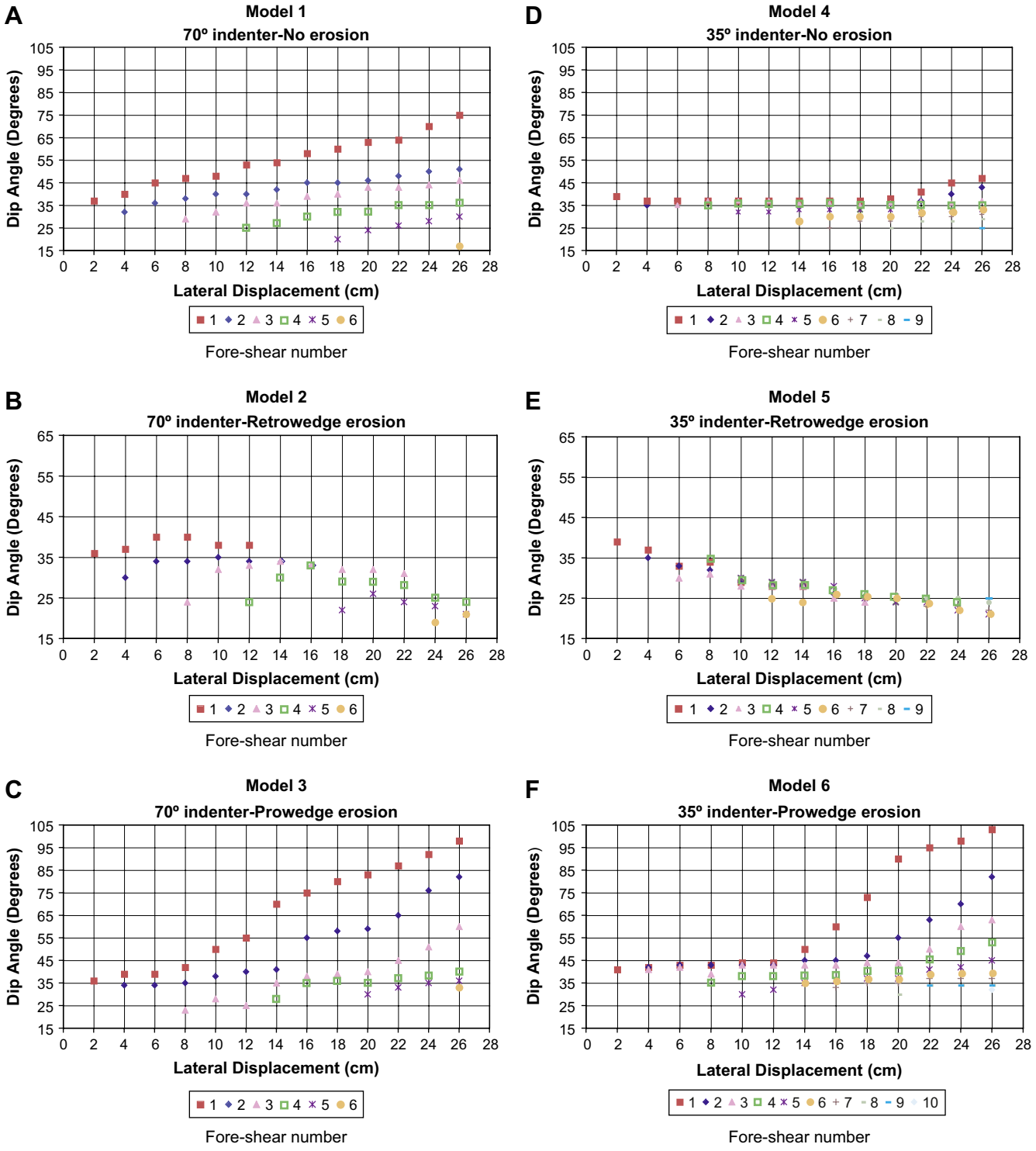

Fig. 6. Plots of the dip of the fore-shears versus lateral displacement, depicting the evolution (rotation) of individual fore-shears. Note clockwise rotation of passive fore-shears in non-erosion models 1 and 4 (A,D) and prowedge erosion models 3 and 6 (C,F), whereas in retrowedge erosion models 2 and 5 (B,E), the passive fore-shears experienced an overall counter-clockwise rotation.

Conversely, fore-shears in retrowedge erosion models experience an overall counter-clockwise rotation toward the indenter (Fig. 6B and E). Therefore, fore-shears evolve to gently dipping structures in the retrowedge side of those models. While the overall sense of fore-shear rotations is counter-clockwise, individual fore-shears may rotate clockwise during some deformation increments. For example in models deformed with the 70 ° dipping indenter (Fig. 6B), fore-shears rotate clockwise in the early stages but switch to counter-clockwise in the middle stages of the experiment. In

models deformed with the 35 ° dipping indenter (Fig. 6E), fore-shears consistently rotate counter-clockwise throughout the experiment.

3.2. Topography: size and divide migration

The size of the orogen increases steadily through time in the non-erosion models (Figs. 4A and D, 7A and D). The growth of these reference non-erosion wedges (Fig. 7A and D) is self-similar (Davis et al., 1983; Dahlen, 1990), in the sense that the wedges grow in size and keep approximately constant slopes, although the growth is episodic (Mulugeta and Koyi, 1992; Koyi, 1995). The slopes in the retrowedge side of the non-erosion and prowedge erosion models steepen close to the angle of repose (~39 °), and in the retrowedge erosion models, erosion keeps slopes at approximately 35 °. These results are irrespective of the dip of the indenter. The slopes in the prowedge side of the non-erosion and retrowedge erosion models are approximately 32 ° and 22 ° in models deformed with the 70 ° and 35 ° dipping indenters, respectively.

Retrowedge erosion models achieve flux and topographic steady-state conditions after 10–12 cm of lateral displacement (Fig. 4B and E). These conditions are illustrated in the relatively constant topographic profiles in Fig. 7B and E. Similarly, prowedge erosion models reach flux steady-state conditions after 10–12 cm of lateral displacement (Fig. 4C and F), but topographic steady-state was only partially achieved due to progressive increase in wedge width (Fig. 7C and F), confirming that flux and topographic steady-state are independent of each other (Willett and

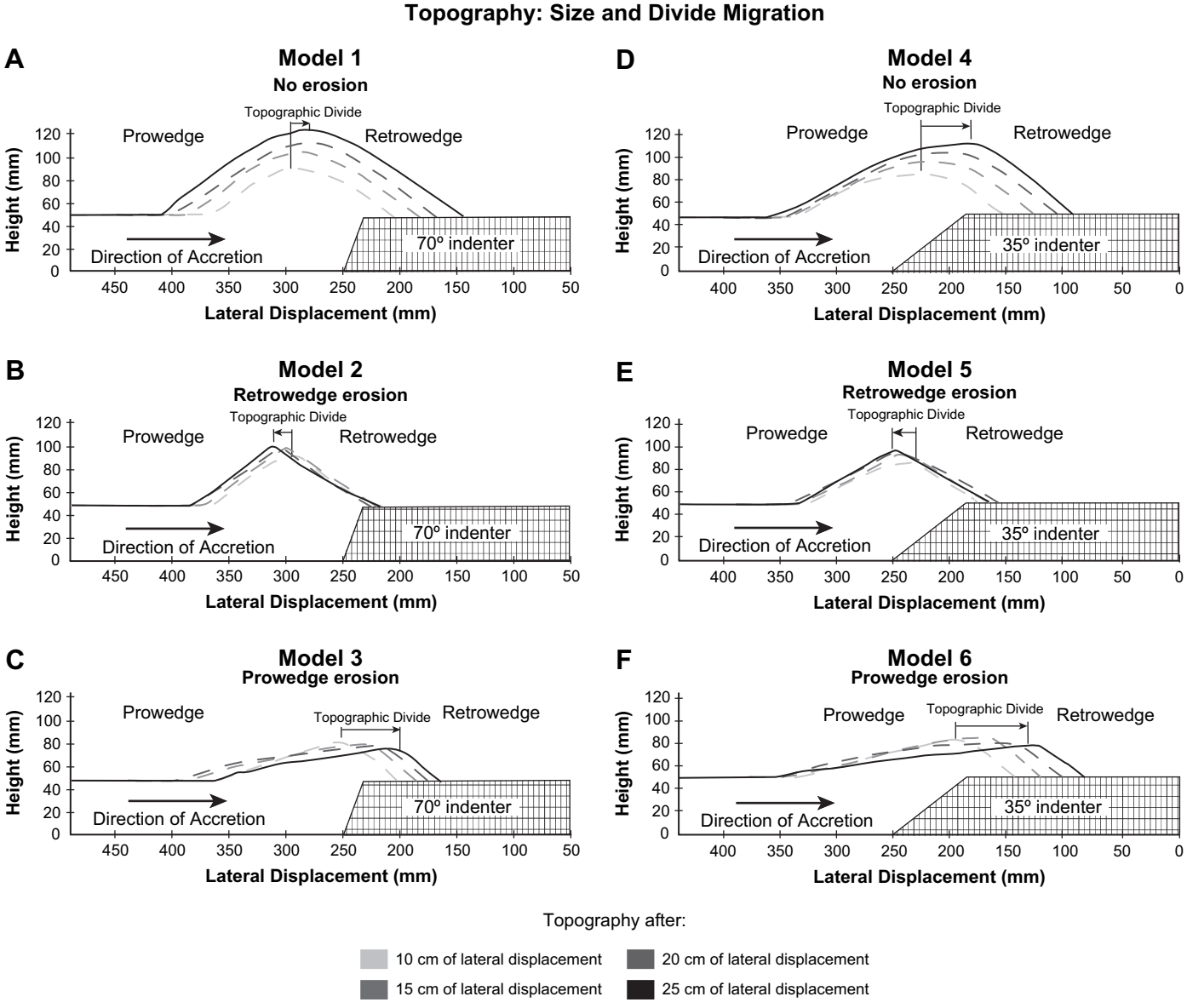

Fig. 7. Topographic features. Size and topographic divide migration of the different models after 10, 15, 20 and 25 cm of lateral displacement. Topographic divide migration was measured using the rigid indenter as a reference location. Note how topography of models (B,E) remains relatively constant after the condition of flux steady-state is achieved. In models (C,F) topography shows more variation.

Brandon, 2002). Models deformed with the 70 ° dipping indenter are always taller and narrower than models deformed with the 35 ° dipping indenter.

The main topographic divide in non-erosion and prowedge erosion models migrates in the direction of the accretionary flux (Fig. 7A, C, D and F), and in our reference frame this movement is toward the rigid indenter. Conversely, in retrowedge erosion models, the main topographic divide migrates in the direction opposite to the accretionary flux, moving away from the rigid indenter. This is true irrespective of the dip of the rigid indenter. The longest migration of topographic divide always occurred in the models deformed with the 35 ° dipping indenter.

3.3. Particle trajectories

Displacement fields for each model were calculated for the intermediate to final stages of lateral displacement after the condition of flux steady-state was achieved. These displacement fields were used to derive particle trajectories assuming a fixed indenter (Fig. 8).

Inclinations of particle trajectories in both erosion models deformed with the 70 ° dipping indenter decrease with depth. Consequently, particle trajectories close to the upper surface of the models are always the steepest (Fig. 8B and C). Conversely, inclinations of particle trajectories in both erosion models deformed with the 35 ° dipping indenter increase with depth in the prowedge side and decrease with depth toward the retrowedge side (Fig. 8E and F). This transition is illustrated in the vector field of Fig. 8E, and it is less obvious in Fig. 8F. Overall inclinations of particle trajectories in non-erosion and 70 ° dipping indenter models are always gentler than those developed in erosion and 35 ° dipping indenter models, respectively.

Inclination of the particle trajectories also varies with erosion location. The steepest particle trajectories are found close

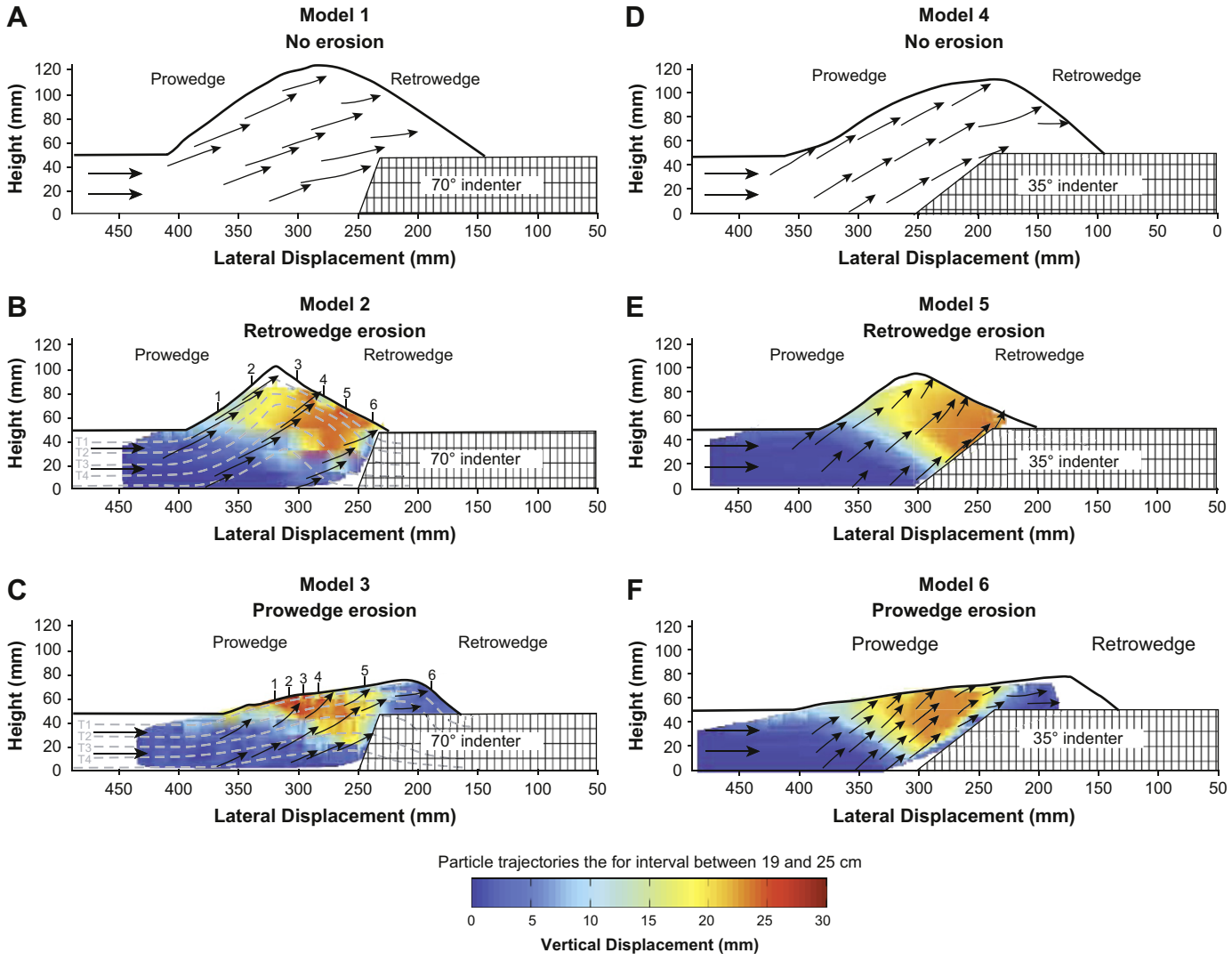

Fig. 8. Particle trajectories derived from the vector field for the interval between 19 and 25 cm of lateral displacement. (B,C) Final stage of four virtual isotherms (dashed lines T1 to T4), surface location of the particles from which thermochronometric ages were calculated (thermochronometric ages shown in Fig. 12), and total vertical displacement for that interval.

to the surface of the retrowedge side in retrowedge erosion models and near the surface of the prowedge side in prowedge erosion models. This trend is illustrated in the vector field of Fig. 8C and E, and is less obvious in Fig. 8B and F.

3.4. Strain

Cumulative maximum shear strain was calculated for each erosion case at different stages of lateral displacement. In Fig. 9, we show strain results after 25 cm of shortening. Cumulative shear strain gamma values range from 0 to >25 (2500%), although the upper boundary of the shear strain color scale in the figures was fixed to a value of 5 (500%) to enhance color contrast within models where strain was substantially less than the maximum shear strain recorded.

Intensity of shear strain and shear band width in models deformed with 70 ° dipping indenters are larger than those deformed with 35 ° dipping indenters. All models produce a progressive increase in width and shear strain intensity of newly formed fore-shears with increasing lateral displacement. However, width and shear strain intensity remain steady after the condition of flux steady-state is reached in both erosion models.

The top of the rigid indenter in non-erosion and prowedge erosion models has areas of concentrated strain associated with a shear plane between the sand paper and the particles. GeoPIV also imaged particles moving down the slope at the upper surface of those models (Fig. 9A, C, D and F).

3.5. Exhumation and thermal modeling

The vertical component of particle motion with respect to the surface, the exhumation and burial of particles (England and Molnar, 1990), was calculated using the GeoPIV software. Positive (exhumation) and negative (burial) values obtained

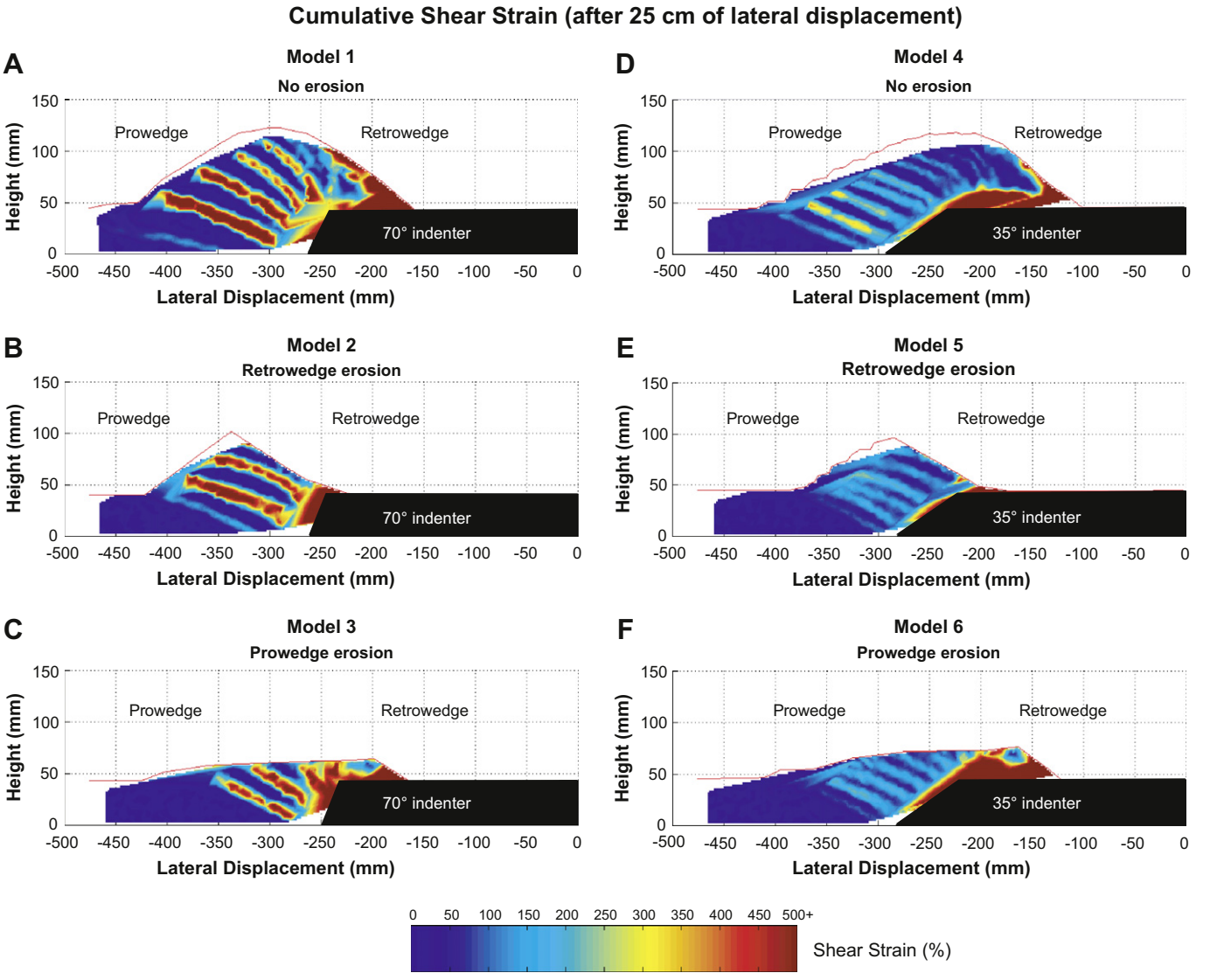

Fig. 9. Cumulative shear strain data for a total lateral displacement of 25 cm. Note that in the models 1–3, the width and the intensity of shear strain associated with the fore-shears are larger than those developed in the models 4–6.

from the analyses range from +40 to −50 mm in all the models (Fig. 10).

Non-erosion models produce little or no exhumation. Erosion models show domains of high exhumation values where erosion is applied (Fig. 10). In erosion models, these domains develop in front of the indenter and migrate progressively in the direction of accretion. In retrowedge erosion models, this migration is less pronounced than in prowedge models.

Normalized exhumation rates, which were obtained normalizing the vertical component of the particle motion with respect to the surface by the amount of convergence required for the uplift, and exhumation/burial history were calculated for 10 PIV-element-patches distributed across the orogen for the 70 ° dipping indenter models (Fig. 11). Elements experience burial followed by exhumation except for particles located immediately in front of the rigid indenter in the upper section, where they experience only exhumation (R5 and P5 in Fig. 11A and B). Elements from retrowedge erosion models reach the greatest depths and exhumation rates.

Exhumation rate variations from the different elements in both erosion models correlate with maximum depth variations. In retrowedge erosion models, maximum exhumation rates and depths are found in the elements originally located in the central section of the orogen and progressively decrease toward the elements in the flanks (Fig. 11C). Originally deeper elements show overall higher exhumation rates. In prowedge erosion models, maximum exhumation rates and depths are found in the elements originally located far from the rigid indenter and progressively decrease toward the elements close to the indenter except for element P6 that probably did not reach

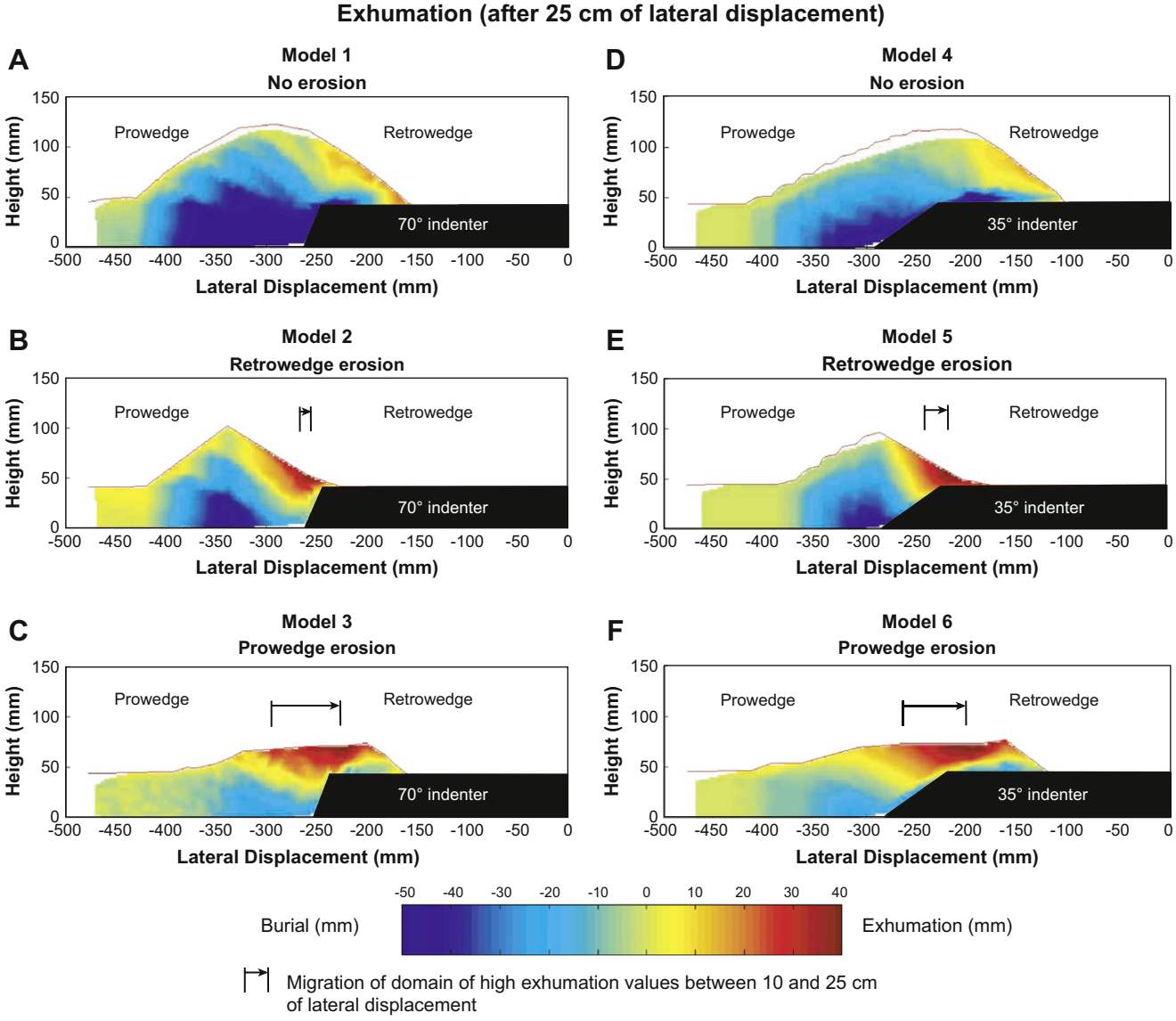

Fig. 10. Exhumation/Burial data for the different models for a total lateral displacement of 25 cm. Note that domains of high exhumation values are linked to places with concentrated erosion. Arrows indicate migration of high exhumation values between 10 and 25 cm of lateral displacement measured with respect to the rigid indenter.

its maximum depth. In these prowedge erosion models, there is no direct correlation between original depth of the particles and exhumation rate.

We used exhumation data and the instantaneous-heating-or-cooling-of-a-semi-infinite-half-space equation (Turcotte and Schubert, 2002), which considers the effect of erosion on subsurface temperatures but neglects lateral heat flow, to analytically calculate the evolution of virtual isotherms (Fig. 8B and C). This relationship is expressed in the following equation:

$$T = T_0 + B \times y + B \times l \times \mathrm{erf}\left\{\frac{y}{\left[2 \times \sqrt{k \times t}\right]}\right\} \quad (2)$$

where T is temperature at the given depth, T_0 is surface temperature, B is the geothermal gradient, y is depth, l is thickness of material removed, erf is the error function, k is thermal diffusivity, and t is time. In our model, we assumed an original geothermal gradient of 25 °C/km, a surface temperature of 25 °C, and a thermal diffusivity of 0.01 cm^2/s. Calculations were performed every 20 frames for a total of 260 frames. Isotherms were assumed to be initially horizontal and equally spaced. Additionally, normalized reset ages of two thermochronometers with closure temperatures of 100 °C and 250 °C, to simulate the accumulation of fission tracks in natural rocks as they are exhumed, were calculated for both erosion models (Figs. 8B, C, and 12). Modeling shows that in both erosion cases the thermochronometric ages are young and converge toward the locus of erosion and become progressively old toward the opposite side. In a natural system, these results may imply a correlation between high exhumation and erosion rates.

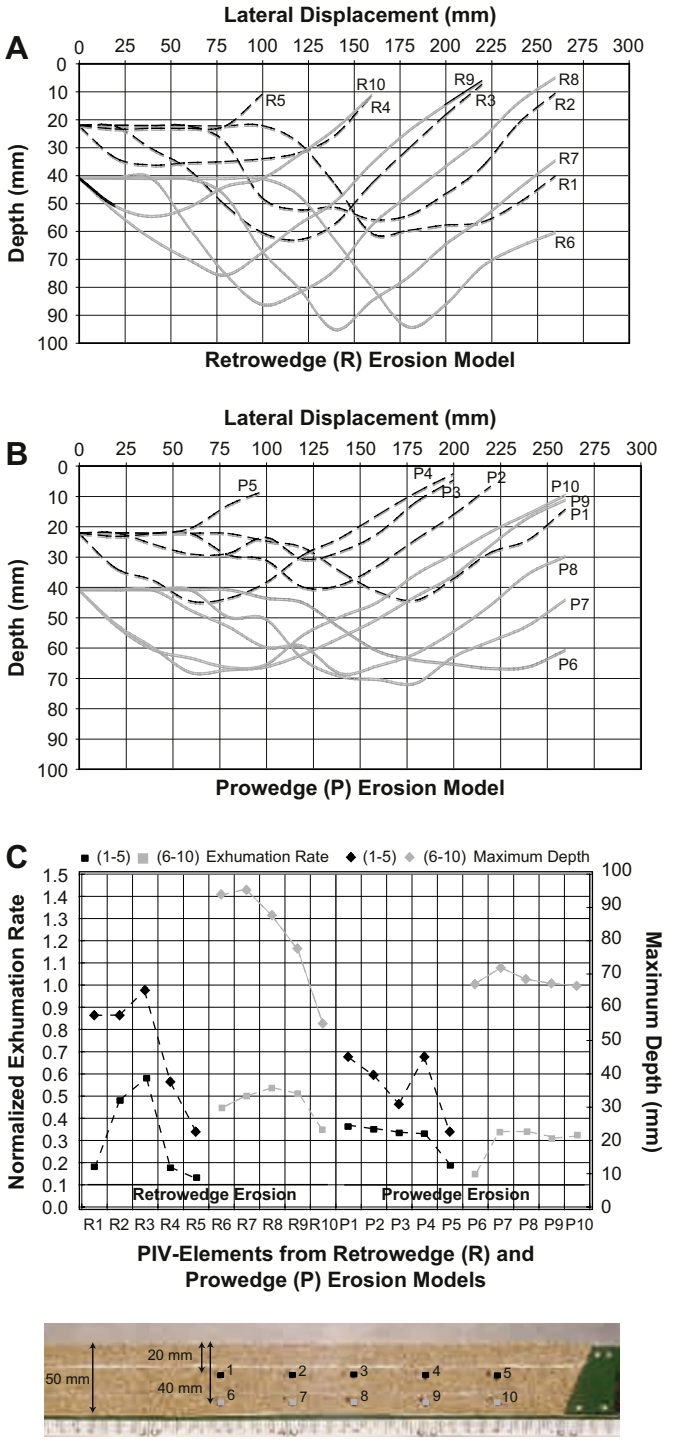

Fig. 11. Depth-time plot of the 10 selected elements in the retrowedge (A) and prowedge (B) erosion models. (C, top) Plot of normalized exhumation rate and maximum depth for the retrowedge and prowedge erosion models. (C, bottom) Photograph of the model showing the initial location of the 10 elements selected for the exhumation rate calculations. Exhumation rate normalized with respect to the lateral displacement.

4. Discussion of results

4.1. (Asymmetric) erosion and steady state

Asymmetric erosion applied to the retrowedge and prowedge side of the experimental orogens produces markedly different kinematics responses. These differences are obvious when comparing the evolution of the passive fore-shears (Figs. 6 and 9) and particle trajectories (Fig. 8). These results are independent of the dip of the rigid indenter.

In the prowedge erosion models, particle trajectories in the upper region of the prowedge side have a larger vertical component (high vertical displacement values in Fig. 8C and F), and steep trajectories than in the retrowedge side. Conversely, in the retrowedge erosion models, particle trajectories in the upper region of the retrowedge side have a larger vertical component than in the prowedge side (Fig. 8B and E). In such a displacement field, passive and relatively linear fore-shears will rotate clockwise as they are transported up the ramp in the prowedge erosion models and counter-clockwise in the retrowedge erosion models. These results imply that vertical unloading due to concentrated erosion leads to steep particle trajectories, erosion's pull effect of Pinter and Brandon (1997). This effect enhances vertical over lateral extrusion and affects the sense of rotation of fore-shears, which produces gently dipping structures in the retrowedge erosion models and steeply dipping and even overturned structures in the prowedge erosion models. These results suggest that the attitude of fault-like structures, in the absence of other processes that

could affect fault-dip, may be used as a first-order approximation to distinguish between orogens where erosion has been concentrated in the prowedge or in the retrowedge. Overturning of beds, faults, and fold axes, with a sense of rotation similar to the one observed in our prowedge erosional models, have been reported in restored profiles of the Olympics Mountains (Tabor and Cady, 1978), which has also been identified as an area where erosion is concentrated in the prowedge and coupled to tectonic (Willett, 1999). Similarly, fabric rotation, resulting from stress changes and asymmetric particle path across the orogenic divide, has been reported in the erosive and topographic-steady-state doubly-vergent wedge of Taiwan (Fisher et al., 2007). In this natural orogen, material is supposedly accreted in the prowedge, buried, and deeply exhumed in the retrowedge (Willett and Brandon, 2002). Systematic overprinting relationships and cleavage pattern support this hypothesis (Fisher et al., 2007).

In the erosion models, once the conditions of flux and topographic steady-state are achieved, the initial dip angle of the fore-shears and the spacing remain constant. This pattern is consistent throughout the models and takes place irrespective of the dip of the rigid indenter. This behavior is probably the result of a relatively constant cross-sectional distribution of vertical load after topographic steady-state (Fig. 7). Under these conditions there are not more perturbations to the gravitational stresses (mechanical equilibrium) and the fore-shears in the wedge form at constant spacing and with similar dips.

Orogenic width growth in our experiments is limited by the change in the dip of the active fore-shear and erosion in the retrowedge side. In the retrowedge erosion models, after the conditions of topographic and flux steady-state are reached, the dip of the active fore-shear remains constant and erosion limits wedge growth in the retrowedge, fixing the width of the wedge. In the prowedge erosion models, although the dip of the active fore-shear is similar to the retrowedge erosion models after reaching steady-state conditions, the wedge grows slightly wider because erosion does not prevent material from moving toward the retrowedge. These results suggest that in our experiments, after flux steady-state conditions, orogenic width is fully controlled by erosion or the lack of it. Analytical models have also shown that erosion, among other variables, controls orogenic width (Hilley and Strecker, 2004; Whipple and Meade, 2004).

Topographic-divide migration and size of the orogen is also partially controlled by erosion. In the non-erosion cases, the wedge grows without limitations as new material is accreted, and the topographic divide migrates in the direction of tectonic accretion. Theoretically, orogenic growth should be limited by the strength of the ''crust'' before it collapses under its own weight (Rey et al., 2001), and the shape of the orogen should be entirely dictated by wedge mechanics (Chapple, 1978; Davis et al., 1983; Suppe, 1981; Dahlen et al., 1984; Koons, 1990). In the erosion models, despite the fact that we applied erosion approximately parallel to the natural slope at constant lateral displacement intervals, our erosion rule may have affected the self-similar growth (Davis et al., 1983; Dahlen, 1984) and produced periods of subcritical growth or disequilibrium wedge shapes during its evolution (Suppe, 1981; Davis et al., 1983), which may explain variations in the topographic taper between models. Under these conditions, the topographic divide in the erosion models always migrated in the direction of the erosion wave irrespective of the direction of accretion or convergence, suggesting that erosion plays a more important role than direction of tectonic accretion during orogenic evolution of the experimental wedge. In this context, our results agree with the numerical models of Willett (1999), in which high erosion rates produced migration of the topographic divide in the direction of erosion.

In our experiments, both erosion models produced one more fore-shear than non-erosion cases irrespective of the erosion side, thus reducing the lifetime activity of the fore-shears. If we were to increase the shortening of the model over the 40% achieved, we would probably see a difference of more than one fore-shear between erosion and non-erosion cases based on the trend of Fig. 4. These results disagree with some of the results reported by Persson and Sokoutis (2002), in which erosion prolonged the activity of the shear bands in all cases except the cases with the 15 ° and 30 ° dipping indenter with total erosion producing at least one additional shear band. Neither of those experiments probably reached topographic and flux steady-state, thus the cross-sectional distribution of vertical loads probably changed over time. Flux and topographic steady-state in our experiments limited the expected pattern of increased spacing between shear bands as the orogen grew (Figs. 4 and 5), thus more shear bands are generated in our erosion and steady-state models.

4.2. Thermal implications

Overall, the particles move faster through the isotherm in the side of the orogen where erosion is concentrated, either prowedge or retrowedge side, moving with a trajectory increasingly normal to the isotherms, as shown in Fig. 8B and C. However, in the prowedge erosion model, particles near the active fore-shear in the hanging-wall tend to move faster through the isotherms than the rest of the wedge. Once the fore-shear becomes inactive, the particles slow down and remain relatively steady at the same structural level as they are slowly brought to the surface. Then the particles near the newly formed fore-shear in the hanging-wall speed up similar to the previous cycle of fore-shear formation. This behavior explains the young thermochronometric ages located in front of the wedge (1 in Figs. 8C and 12), where the fore-shear is active, and not in the central part of the prowedge toward the topographic divide, where fore-shears are extinct and deeply exhumed particles are being highly eroded (Fig. 10C and F). Conversely, in the retrowedge erosion models, particle velocities with respect to the isotherms in the retrowedge side do not seem to be directly affected by the active fore-shears. Instead since the isotherms are advected toward the central part of the surface of the retrowedge side and particles move relatively perpendicular to the isotherm at similar velocities, the youngest thermochronometric ages are found in the central section of the retrowedge (4 and 5 in Fig. 8B).

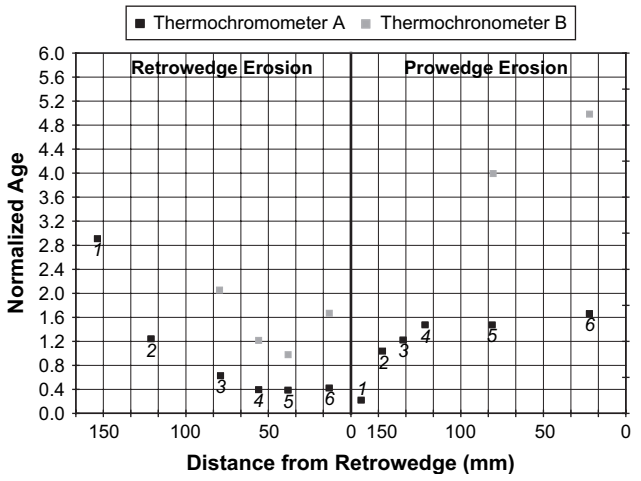

Fig. 12. Plot of the normalized age versus distance for two thermochronometers (T1 and T3 in Fig. 8B and C) for the erosion models. Ages normalized with respect to lateral displacement. Some ages from thermochronometer B are not shown because they were not reset. Surface location of particles (italic numbers) shown in Fig. 8.

Ages of the two thermochronometers in the retrowedge erosion models tend to converge and become younger toward the elements 4 and 5 in the retrowedge (Fig. 12). One could interpret this tendency as rapid exhumation, in the absence of accurate particles trajectories. However, exhumation rates in this region are very similar but the isotherms are deflected toward the surface, producing compressed young ages as particles pass through the closely spaced isotherms. These results illustrate the complex relationship between isotherms, particle position at any given time, and thermochronometric ages in orogenic wedges. These results suggests that caution is needed when interpreting exhumation rates and patterns on the basis of thermochronometry, when particles trajectories are not vertical and isotherms evolve through time. Most thermochronological studies are based, for simplification, on 1-D vertical particle trajectories (Stüwe and Barr, 1998), but as shown in the work of Batt and Brandon (2002) and in this experiment, particle trajectories involve at least considering lateral (2-D) motion. We found no direct correlation between surface patterns of deeply exhumed particles and thermochronometric ages. However, particles that reached maximum depths, experience the highest exhumation rates, irrespective of their original crustal level.

4.3. Control of the dip angle of the indenter

Steeply dipping indenters produce overall gentle trajectories and relatively narrow orogens, and gently dipping indenters favor overall steep trajectories and relatively wide orogens. A possible explanation of this observation is that steeply dipping indenters are more effective than gently dipping indenters at accreting material laterally. Shear stresses at the surface of the indenter (ramp) in the 70 ° dipping indenter models are insufficient to surpass resistance to sliding, when compared to the 35 ° dipping indenter models. Therefore, in models with steeply dipping indenters, material is effectively transferred horizontally to the front of the indenter as deformation progresses, producing overall gentle particle trajectories and preventing the orogen growth toward the retrowedge. This interpretation may also explain why the back-shear of the 70 ° dipping indenter models is not along the ramp of the indenter but away from its tip (Fig. 3A), forming an effective indenter (Persson and Sokoutis, 2002). In contrast, in models with gently dipping indenters, material is efficiently transported up the ramp, producing overall steep particle trajectories and a wider orogen, since material moves easily toward the retrowedge. Several experiments have reported similar lateral compaction behavior for models with ramps dipping $\geq$60 ° (Bonini et al., 1999; Persson, 2001) and $\leq$30 ° (Persson, 2001).

Sandbox experiments (Liu et al., 1992; Marshak and Wilkerson, 1992; Persson; 2001) have shown an inverse relationship between the vertical load and number of shear bands developed due to variations in the force needed to cause movement along the shear bands and in the cohesion of the material (Mulugeta, 1988). Under the accretion conditions developed in our experiment, the vertical distribution of load differs greatly between the two indenter models. This difference may explain the differences in the total number, spacing, intensity of shear strain, and width of the shear plane of the fore-shears. The prowedge sides of the models with steeply dipping indenters (70 °) are progressively taller than the prowedge sides of the gently dipping indenter models (35 °), thus vertical load increases. Therefore, deformation in the former is propagated toward the front of the indenter primarily in the form of lateral compaction, with fewer and long-lived fore-shears with highly sheared and wide shear planes that develop at longer spacing. Conversely, deformation in the latter is propagated to the front of the indenter primarily in the form of numerous and short-lived fore-shears with slightly sheared and narrow shear planes that develop at shorter spacing.

Results also showed that the initial dip angle of the fore-shears is shallower in models with steeply dipping indenters compared to models with gently dipping indenters. According to Coulomb theory (Davis et al., 1983; Dahlen et al., 1984), the initial failure plane is located at an angle of $\pm(45-\varphi/2)$ with respect to the principal stress axis, where φ is the angle of internal friction. Therefore, lowering the dip of the indenter should increase the inclination of the principal stress axis, which agrees with the experimental observations.

5. Conclusions

Our experiments were conducted to explore the interaction between tectonic and surface processes in doubly-vergent orogenic wedges, allowing for inherent limitations and assumptions.

- Asymmetric erosion applied to the experimental doubly-vergent orogens controls internal kinematics. Prowedge erosion leads to rapid clockwise rotation of passive fore-shears, producing steeply dipping and overturned

structures in the retrowedge side. Retrowedge erosion leads to counter-clockwise rotation of passive fore-shears, leading to gently dipping structures in the retrowedge side.
- Erosion applied to either side of our experimental orogen, in combination with the conditions of flux and topographic steady-state, modestly increases the total number of fore-shears, decreases their activity lifetime, and controls size, width, and migration direction of the topographic divide.
- Exhumation rates calculated on the basis of simulated thermochronometry without knowledge of the particles trajectories and thermal structures may result in overestimated rates.
- Dip of the rigid indenter partially controls particle trajectories and strain patterns. Steeply dipping indenters produce overall gentle particle trajectories and relatively few and long-lived fore-shears with highly sheared and wide shear planes. Gently dipping indenters favor overall steep trajectories and numerous and short-lived fore-shears with slightly sheared and narrow shear planes.

Acknowledgements

These experiments were performed at the Saint Anthony Falls Laboratory (SAFL) at the University of Minnesota (UMN). Special thanks to SAFL personnel who made possible calibrations to the experiment and modifications to the apparatus, which was provided by the Department of Civil Engineering (CE) at the UMN. This study benefited from interesting discussions with Prof. Andrew Drescher (CE UMN). We are grateful to Hemin Koyi (Hans Ramberg Tectonic Laboratory, Uppsala University) for providing their ring shear apparatus to measure the frictional properties of the experimental materials and for his helpful comments. We thank Silvan Hoth and Susanne Buiter, for insightful comments that improved this paper, Kelin Whipple for his comments on an early version of this manuscript, and Dyanna Czeck for improving the English and her constructive comments.

Appendix A. Frictional properties of the experimental materials

We measured the frictional properties (friction coefficient and cohesion) of the walnut shells and P400 sand paper, using the experimental apparatus of Maillot and Koyi (2006) designed to measure friction coefficients below ~1000 Pa. We measured the failure envelops of the experimental materials, using the peak shear load values. The reader is referred to Maillot and Koyi (2006), for a detailed description of the apparatus, measurement procedure, and limitations.

The internal friction of the walnut shells and walnut shells against P400 sand paper were calculated from a linear regression of the data with error bars (Fig. A1). The walnut shells have an internal friction of 0.83 ± 0.02 (friction angle 38.5–40.8 °) and cohesion of 23 ± 13 Pa (Fig. A1, top), and the walnut shells against the P400 sand have an internal friction of 0.73 ± 0.01 (friction angle 35.6–36.7 °), and cohesion of 80 ± 13 Pa (Fig. A1, bottom).

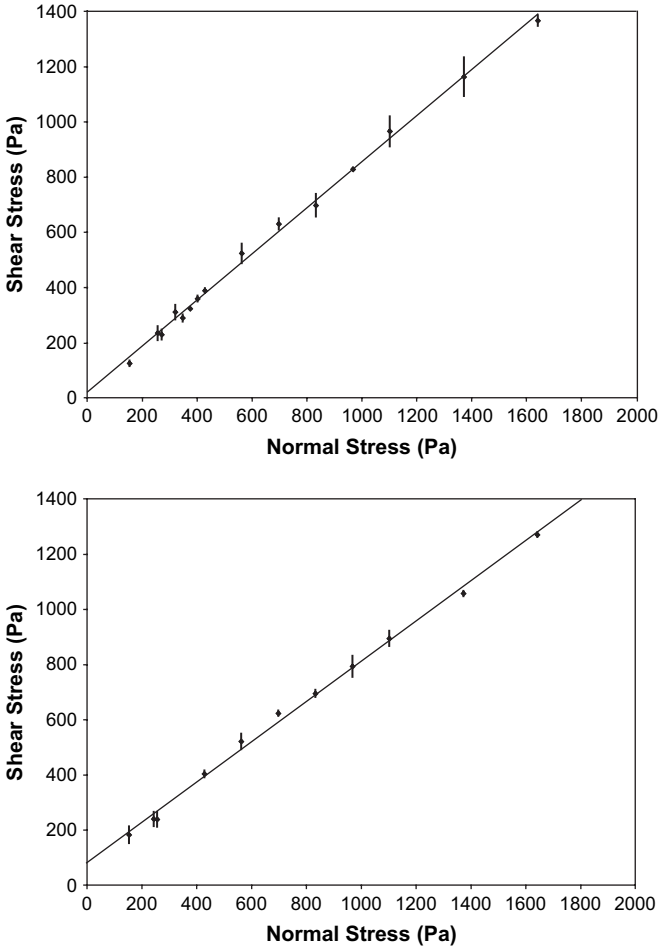

Fig. A1. (Top) Failure envelop for the walnut shells. A linear regression gives $\tau = (0.83 \pm 0.02)\ \tau_n + 23 \pm 13$ (friction angle between 38.5 ° and 40.8 °). (Bottom) Failure envelop for the walnut shells against P400 sand paper. A linear regression gives $\tau = (0.73 \pm 0.01)\ \tau_n + 80 \pm 13$ (friction angle between 35.6 ° and 36.7 °).

References

Adam, J., Hoth, S., Kukowski, N., Oncken, O., 2002. Strain variation and partitioning in thrust wedges: high-resolution data from scaled sandbox experiments by 2D-3D PIV analysis. Bollettino di Geofisica teorica ed applicata 42 (1/2), 123–126.

Adam, J., Urai, J., Wieneke, B., Oncken, O., Pfeiffer, K., Kukowski, N., Lohrmann, J., Hoth, S., Van der Zee, W., Schmatz, J., 2005. Shear localisation and strain distribution during tectonic faulting – new insights from granular-flow experiments and high-resolution optical image correlation techniques. Journal of Structural Geology 27 (2), 283–301.

Adams, J., 1980. Contemporary uplift and erosion of the Southern Alps, New Zealand. GSA Bulletin 91, 1–114.

Avouac, J., Burov, E., 1996. Erosion as a driving mechanism of intracontinental mountain growth. Journal of Geophysical Research 101 (B8), 17747–17769.

Barr, T., Dahlen, F., 1989. Brittle frictional mountain building, 2. Thermal structure and heat budget. Journal of Geophysical Research 94 (B4), 3923–3947.

Batt, G., Brandon, M., 2002. Lateral thinking: 2-D interpretation of thermochronology in convergent orogenic settings. Tectonophysics 239, 185–201.

Beaumont, C., Jamieson, R., Nguyen, M., Lee, B., 2001. Himalayan tectonics explained by extrusion of a low-viscosity crustal channel coupled to focused surface denudation. Nature 414, 738–742.

Beaumont, C., Fullsack, P., Hamilton, J., 1992. Erosional control of active compressional orogens. In: McClay, K.R. (Ed.), Thrust Tectonics. Chapman and Hall, London, pp. 1–18.

Bonini, M., Sokoutis, D., Talbot, C., Boccaletti, M., Milnes, A., 1999. Indenters growth in analogue models of Alpine-type deformation. Tectonics 18, 119–128.

Brandon, M.T., Roden-Tice, M.K., Garver, J.I., 1998. Late cenozoic exhumation of the Cascadia accretionary wedge in the Olympics Mountain, Northwest Washington State. GSA Bulletin 110, 985–1009.

Chapple, W., 1978. Mechanics of thin-skinned fold-and-thrust belts. GSA Bulletin 89, 1189–1198.

Cobbold, P., Davy, P., Gapais, D., Rossello, E., Sadybakasov, E., Thomas, J., Tondji Biyo, J., de Urreiztieta, M., 1993. Sedimentary basins and crustal thickening. Sedimentary Geology 86, 77–89.

Colletta, B., Letouzey, J., Pinedo, R., Ballard, J.F., Balé, P., 1991. Computerized X-ray tomography analysis of sandbox models: examples of thin-skinned thrust systems. Geology 19 (11), 1063–1067.

Davis, D., Suppe, J., Dahlen, F., 1983. Mechanics of fold-and-thrust belts and accretionary wedges. Journal of Geophysical Research 88, 1153–1172.

Dahlen, F., Suppe, J., Davis, D., 1984. Mechanics of fold-and-thrust belts: cohesive Coulomb theory. Journal of Geophysical Research 88, 1153–1172.

Dahlen, F., 1990. Critical taper model of fold-and-thrust belts and accretionary wedges. Annual Reviews in Earth and Planetary Sciences 18, 55–99.

Dahlen, F., 1984. Non cohesive critical coulomb wedges: an exact solution. Journal of Geophysical Research 89, 10125–10133.

Dahlen, F., Suppe, J., 1988. Mechanics, growth, and erosion of mountain belts. GSA Special Paper 218, 161–178.

Dahlen, F., Barr, T., 1989. Brittle frictional mountain building, 1. Deformation and mechanical energy budget. Journal of Geophysical Research 94 (B4), 3906–3922.

Dahlen, F., 1988. Mechanical energy budget of a fold-and-thrust belt. Nature 331, 335–337.

Ellis, S., 1995. Continental convergence: length scales, aspect ratios, and styles of crustal deformation. PhD thesis, Dalhousie University.

England, P., Houseman, G., 1986. Finite strain calculations of continental deformation, 2. Comparison with the India–Asia collision zone. Journal of Geophysical Research 91, 3664–3676.

England, P., Molnar, P., 1990. Surface uplift, uplift of rocks, and exhumation of rocks. Geology 18, 1173–1177.

Finlayson, D., Montgomery, D., Hallet, B., 2002. Spatial coincidence of rapid inferred erosion with young metamorphic massifs in the Himalayas. Geology 30, 219–222.

Fisher, D.M., Willett, S., En-Chao, Y., Clark, M.B., 2007. Cleavage fronts and fans as reflections of orogen stress and kinematics in Taiwan. Geology 35 (1), 65–68.

Goodman, R.E., 1988. Introduction to rock mechanics. Wiley, New York.

Hilley, G., Strecker, M., 2004. Steady-state erosion of critical coulomb wedges with applications to Taiwan and the Himalaya. Journal of Geophysical Research, doi:10.1029/2002JB002284. Solid Earth 109.

Hoth, S., Adam, J., Kukowski, N., Oncken, O., 2006. Influence of erosion on the kinematics of bivergent orogens: results from scaled sandbox simulations. In: Willett, S.D., Hovius, N., Brandon, M.T., Fisher, D.M. (Eds.), Tectonics, Climate, and Landscape Evolution. Geological Society of America Special Paper 398, Penrose Conference Series, pp. 201–225, doi:10.1130/2006.2398(12).

Howard, A., 1994. A detachment-limited model of drainage basin evolution. Water Resources Research 30 (7), 2261–2285.

Hubbert, M.K., 1937. Theory of scale models as applied to the study of geologic structures. GSA Bulletin 48, 1459–1520.

Jamieson, R., Beaumont, C., Nguyen, M., Lee, B., 2002. Interaction of metamorphism, deformation, and exhumation in large convergent orogens. Journal of Metamorphic Geology 20, 1–16.

Konstantinovskaia, E., Malavieille, J., 2005. Erosion and exhumation in accretionary orogens: experimental and geological approaches, Geochemistry. Geophysics, Geosystems 6, doi:10.1029/2004GC000794. Q02006.

Koyi, H., 1997. Analogue modeling: from a qualitative to a quantitative technique, a historical outline. Journal of Petroleum Geology 20 (2), 223–238.

Koyi, H., 1995. Mode of internal deformation in sand wedges. Journal of Structural Geology 17, 293–300.

Koyi, H., Hessami, K., Teixell, A., 2000. Epicenter distribution and magnitude of earthquakes in fold-thrust belts: insights from sandbox models. Geophysical Research Letters 27 (2), 273–276.

Koons, P., 1987. Some thermal and mechanical consequences of rapid uplift: an example from the Southern Alps, New Zealand. Earth and Planetary Science Letters 86, 307–319.

Koons, P., 1990. The two sided wedge in orogeny: erosion and collision from the sand box to the Southern Alps, New Zealand. Geology 18, 679–682.

Koons, P.O., Zeitler, P.K., Chamberlain, C.P., Craw, D., Meltzer, A.S., 2002. Mechanical links between erosion and metamorphism in Nanga Parbat, Pakistan Himalaya. American Journal of Science 302 (9), 749–773.

Leturmy, P., Mugnier, J., Vinour, P., Baby, P., Colletta, B., Chabron, E., 2000. Piggyback basin development above a thin-skinned thrust belt with two detachment levels as a function of interactions between tectonic and superficial mass transfer: the case of the Subandean Zone (Bolivia). Tectonophysics 320, 45–67.

Liu, H., McClay, K.R., Powell, D., 1992. Physical models of thrust wedges. In: McClay, K.R. (Ed.), Thrust Tectonics. Chapman and Hall, London, pp. 71–81.

Lohrman, J., Kukowski, N., Adam, J., Oncken, O., 2003. The impact of analogue material properties on the geometry, kinematics and dynamics of convergent sand wedges. Journal of Structural Geology 25, 1691–1711.

Maillot, B., Koyi, H., 2006. Thrust dip and thrust refraction in fault-bend folds: analogue models and theoretical predictions. Journal of Structural Geology 28 (1), 36–49.

Malavieille, J., 1984. Modélisation expérimentale des chevauchements imbriqués: Application aux chaines de montagnes. Bulletin de la Societé Géologique de France 7, 129–138.

Mandl, G., 1988. Mechanics of tectonic faulting. Models and Basic Concepts. Elsevier, Amsterdam.

Marshak, S., Wilkerson, M., 1992. Effect of overburden thickness on thrust belt geometry and development. Tectonics 11, 560–566.

Merle, O., Abidi, N., 1995. Approche expérimentale du fonctionnement des rampes emergentes. Bulletin de la Société Géologique de France 166, 439–450.

Mulugeta, G., 1988. Modelling the geometry of Coulomb thrust wedges. Journal of Structural Geology 10, 847–859.

Mulugeta, G., Koyi, H., 1987. Three-dimensional geometry and kinematics of experimental piggyback thrusting. Geology 15, 1052–1056.

Mulugeta, G., Koyi, H.A., 1992. Episodic accretion and strain partitioning in a model sand wedge. Tectonophysics 202, 319–333.

Pazzaglia, F.J., Brandon, M.T., 2001. A fluvial record of long-term steady-state uplift and erosion across the Cascadia forearc high, western Washington state. American Journal of Science 301, 385–431.

Peltzer, G., Tapponnier, P., 1988. Formation and evolution of strike slip faults, rifts, and basins during India–Asia collision: an experimental approach. Journal of Geophysical Research 93, 15085–15117.

Persson, K., 2001. Effective indenters and the development of double-vergent orogens: insights from analogue sand models. In: Koyi, H., Mancktelow, N. (Eds.), Tectonic Modeling A: Volume in Honor of Hans Ramberg, 193. Geological Society of America, pp. 191–206.

Persson, K., Sokoutis, D., 2002. Analogue models of orogenic wedges controlled by erosion. Tectonophysics 356, 323–336.

Persson, K., Garcia-Castellanos, D., Sokoutis, D., 2004. River transport effects on compressional belts: first results from an integrated analogue–numerical model. Journal of Geophysical Research 109, doi:10.1029/2002JB002274. B01409.

Pinter, N., Brandon, M., 1997. How erosion builds mountains. Scientific American 276 (4), 74–79.

Raffel, M., Willert, C., Kompenhans, J., 1998. Particle image velocimetry. Berlin Heidelberg. Springer, New York.

Ramberg, H., 1967. Model experimentation of the effects of gravity on tectonics processes. The Geophysical Journal of the Royal Astronomical Society 14, 307–329.

Reiners, P., Ehlers, T., Garver, J., Gran-Mitchell, S., Montgomery, D., Vance, J., Nicolescu, S., 2002. Late Miocene exhumation and uplift of the Washington Cascades. Geology 30, 767–770.

Rey, P., Vanderhaeghe, O., Teyssier, C., 2001. Gravitational collapse of the continental crust: definition, regimes and modes. Tectonophysics 342, 435–449.

Schreurs, G., Buiter, S., Boutelier, D., Corti, G., Costa, E., Cruden, A., Daniel, J.-M., Hoth, S., Koyi, H., Kukowski, N., Lohrmann, J., Ravaglia, A., Schlische, R.W., Withjack, M.O., Yamada, Y., Cavozzi, C., DelVentisette, C., Elder Brady, J., Hoffmann-Rothe, A., Mengus, J.-M., Montanari, D., Nilforoushan, F., 2006. Analogue benchmarks of shortening and extension experiments. In: Buiter, S.J.H., Schreurs, G. (Eds.), Analogue and Numerical Modelling of Crustal-Scale Processes. Special Publication 253. Geological Society, London, pp. 1–27.

Stüwe, K., Barr, T., 1998. On uplift and exhumation during convergence. Tectonics 17, 80–88.

Schellart, W., 2000. Shear test results for cohesion and friction coefficients for different granular materials: scaling implications for their usage in analogue modeling. Tectonophysics 324, 1–16.

Sonder, L., England, P., 1986. Vertical averages of rheology of the continental lithosphere: relation to thin sheets parameters. Earth and Planetary Science Letters 77, 81–90.

Suppe, J., 1981. Mechanics of mountain building and metamorphism in Taiwan. Memoir of the Geological Society of China 4, 67–89.

Tabor, R.W., Cady, W.M., 1978. The structure of the Olympic Mountains, Washington–analysis of a subduction zone. US Geological Survey Professional Paper 1033.

Turcotte, D., Schubert, G., 2002. Geodynamics, second ed. Cambridge University Press.

White, D., Take, W., Bolton, M., 2003. Soil deformation measurement using particle image velocimetry (PIV) and photogrammetry. Geotechnique 53 (7), 619–631.

Willett, S., 1999. Orography and Orogeny: the effects of erosion on the structure of mountain belts. Journal of Geophysical Research 104 (B12), 28957–29981.

Willett, S., Beaumont, C., Fullsack, P., 1993. A mechanical model for the tectonics of doubly verging compressional orogens. Geology 21, 371–374.

Willett, S., Brandon, M., 2002. On steady state in mountain belts. Geology 30, 175–178.

Whipple, K., Meade, B., 2004. Controls on the strength of coupling among climate, erosion, and deformation in two-sided, frictional orogenic wedges at steady state. Journal of Geophysical Research-Earth Surface 109, 1–24.

Whipple, K., Tucker, G., 1999. Dynamics of the stream-power river incision model: implications for height limits of mountain ranges, landscape response timescales, and research needs. Journal of Geophysical Research 104 (B8), 17661–17674.

Yui, T.F., Chu, H.T., 2002. Possible factors affecting the topography of the Backbone Range of Taiwan. Western Pacific Earth Sciences 2, 105–118.

Zeitler, P., Koons, P., Bishop, M., Chamberlain, C., Craw, D., Edwards, M., Hamidullah, S., Jan, M., Khan, M., Khattak, M., Kidd, W., Mackie, R., Meltzer, A., Park, S., Pecher, A., Poage, M., Sarker, G., Schneider, D., Seeber, L., Shroder, J., 2001. Crustal reworking at Nanga Parbat, Pakistan: metamorphic consequences of thermal–mechanical coupling facilitated by erosion. Tectonics 20 (5), 712–728.